



OpenFOAM analysis of the wave radiation by a box-type floating structure

H. Islam, S.C. Mohapatra, J. Gadelho, C. Guedes Soares^{*}

Centre for Marine Technology and Ocean Engineering (CENTEC), Instituto Superior Técnico, Universidade de Lisboa, Portugal

ARTICLE INFO

Keywords:

OpenFOAM
Wave radiation
Response amplitude operator
Wave forces

ABSTRACT

Wave radiation due to heave, surge, and pitch by a box-type floating structure based on computational fluid dynamics (CFD) simulations using OpenFOAM is analysed. The CFD simulation results include surge and heave forces and response amplitude operator for the heave, surge, and pitch at different wave lengths. The numerical simulation results of heave force due to incoming waves and resulting motion are compared against experimental data and linearized analytical solutions based on velocity potential flow theory. The hydrodynamic effect on the width and draft of the structure in analytical results for vertical wave force, horizontal wave force, and torque are studied whilst, the effect of different wave lengths on heave, surge and pitch forces and response amplitude operator from CFD results are analysed. The comparison shows that the CFD results are in good agreement with the experimental ones and are very close to the analytical ones. The paper concludes that CFD is well capable of simulating wave interaction behaviour of a box-type floating structure for wave energy converters, and the developed analytical model can serve as an efficient middle-fidelity performance evaluation tool for such structures during design development stage.

1. Introduction

Over the last decade, there has been a significant interest on CFD modelling a large number of engineering problems associated with fluid-structure interaction due to its level of accuracy and efficiency in handling of complex problems arising in marine and ocean engineering. However, there is little progress in the literature of wave interaction with floating bodies, incorporating different motion characteristics for designing wave energy converters. Due to the recent advances in computational modelling, CFD simulations can give deeper insight into the floating body hydrodynamics, which can facilitate better design and optimized operating setup.

CFD is one of the popular approaches for modelling hydrodynamic loads on the floating structures of different geometries. CFD methods, which are based on solving Navier-Stokes equations, if properly solved, can capture most of the nonlinear hydrodynamic loads on an offshore structure and can lead to very reliable results. Therefore, recently, the scientific community is interested in comparing the results of motion characteristics of floating structures of various geometries obtained from CFD simulations against experimental data and analytical results to set benchmarks.

Box-type floating structures are frequently used as breakwaters for small harbours and marinas (Black et al., 1971; Drimer et al., 1992;

Sannasiraj et al., 1995; Williams et al., 2000; Huang et al., 2015). The study of the radiation problem of box-type floating structures based on CFD modelling are of recent interest, as it can provide the fundamental information about the structures regarding the hydrodynamic characteristics of added mass, radiation damping coefficients, and wave forces. Under the excitation of waves, a rigid floating body will exhibit six degrees of freedom, namely three translations (heave, sway and surge) and three rotational motions (pitch, yaw and roll). Practically, vertical, horizontal and rotational motions are of primary importance for the hydrodynamic analysis of a floating structure for designing wave energy converters.

Recently, several researchers have studied floating structures and wave energy converters based on CFD models. Holmes et al. (2001) used CFD to predict the hydrodynamic loads on heave plates in simple harmonic motion and least mean square method was used to obtain the appropriate Morison coefficients for the plates under variety of sea conditions. Jung et al. (2013) studied numerically the interaction between a regular wave and a roll motion of a rectangular floating structure using VOF method based on the finite volume method. The results showed good agreement with potential theory and also effectively represented the process of vortex generation. Philip et al. (2013) studied the heave damping effects due to circular plates attached to spar hull based on experimental investigation and CFD simulation to establish the

^{*} Corresponding author.

E-mail address: c.guedes.soares@centec.tecnico.ulisboa.pt (C. Guedes Soares).

relationship between wave frequencies and damping ratio. They observed that increase in added mass combined with viscous damping is a key factor for the effectiveness of heave plates in reducing motion response of spar platforms, which was also identified by Lavrov and Guedes Soares (2016). Chen et al. (2014) simulated the wave induced roll of a 2D rectangular barge using OpenFOAM in beam sea conditions and the results were validated with experimental results. They concluded that viscous effect not only can damp out the roll motion but also can increase it. Connell and Cashman (2015) compared the heave response of a freely floating body between a state-space mathematical model and a Navier-Stokes (N-S) based time domain CFD program, ANSYS Fluent. They conclude that a combined approach using both the models can make floating body study more efficient and less time consuming. Jaswar et al. (2015) compared the semi-submersible heave motion response prediction among diffraction, diffraction-viscous and diffraction-Morison methods based on diffraction potential flow theory. The paper concluded that Morison equation based drag correction method is able to estimate heave response in damping dominated regions and provides more reasonable motion tendency compared to other methods. Paci et al. (2016) simulated the dynamics of a floating vertical cylinder, moored to the bottom, under regular waves, using OpenFOAM coupled with IHFOAM. They concluded that OpenFOAM coupled with IHFOAM is a reliable tool for studying floating body dynamics. However, they mentioned that dynamic mesh approach for unmoored structures in OpenFOAM is complicated. Later, Antonini et al. (2016, 2016a) used overset meshing technique from Star-CCM + to simulated OXYFLUX model's dynamic response and pumping performance in regular waves. Apart from validation study, the papers also highlighted the effect of non-linearity in such studies. Devolder et al. (2017) simulated the heaving floating point absorber wave energy converters using OpenFOAM based on two-phase Navier-Stokes fluid solver coupled with a motion solver. He modified the built in SST k- ω turbulence model by implementing a buoyancy term in the turbulent kinetic energy equation to suppress turbulence level at the water and air interface. Bihs et al. (2017) simulated a horizontal cylinder in heave free motion and the motion of a freely floating rectangular barge in waves using the CFD model REEF3D and compared the results with experimental data. They simulated the barge with different grid sizes and reported that a grid size of 0.01 m performed remarkably well. Nematbakhsh et al. (2017) developed and verified a CFD code based on numerical wave tank to study the wave load effects on fixed and floating offshore structures of sway, heave, and roll response. The paper observed that for fixed cylinder, Morison equation performs well for long wave lengths, while for shorter ones, it considerably over predicts the wave loads. On the other hand, Mohapatra et al. (2019) developed a Boussinesq model to study the wave diffraction by a floating fixed truncated vertical cylinder. In this study, they compared the results of wave amplitudes around the cylinder between second-order analytical results with CFD model simulations. Recently, Gadelho et al. (2017) simulated the floating fixed box using OpenFOAM and compared the results against Boussinesq equation based analytical model and experimental results in different cases. Paci and Archetti (2018) studied a spar type floating wind turbine using OpenFOAM coupled with modified boundary conditions and turbulence model. They successfully studied the applicability of the turbine in a particular location, considering the wave history of that place. Islam et al. (2018) also simulated a 3D heaving box in head waves using OpenFOAM and compared the results with linear analytical results and experimental data. However, the box was simulated with only heave free motion and study of wave steepness effect was missing.

On the other hand, the linearized velocity potential flow theory approaches based on analytical solutions for designing floating platforms, wave energy devices and breakwaters are quite reliable and much less computational resource consuming; thus, linearized solutions are still in demand to set benchmarks. Many researchers have been involved in studying the radiation problem of floating structures of different geometries and configurations, to obtain the hydrodynamic coefficients,

wave forces, reflection and transmission coefficients based on analytical/semi-analytical methods (see Lee, 1995; Hsu and Wu, 1997; Zheng et al., 2006; Drobyshevski, 2004). Mohapatra and Guedes Soares (2015) studied the wave forces on a two-dimensional rectangular floating structure based on linearized Boussinesq equations using eigenmode expansion method. Ngina et al. (2015) predicted the wave exciting force on a floating rectangular barge due to surface waves based on panel method with integral equations with the help of appropriate Green's functions. Rodriguez et al. (2016) investigated the numerical nonlinear heave response of a rectangular box concerning on the importance of the relative body dimensions. Further, Rodriguez and Spinneken (2016) performed a series of experiments to analyse the nonlinear loading and dynamic response of a heaving rectangular box in two-dimensions under regular and irregular wave conditions. Recently, Guo et al. (2018) studied the oblique wave diffraction by a long floating structure over flat bottom by analysing the wave forces on the structure and reflection and transmission coefficients in different cases using eigenfunction expansion method.

Generalising further the previous work of Islam et al. (2018), in the present study wave radiation due to heave, surge and pitch motions of box-type floating structure is studied by performing two-dimensional (2D) CFD simulations and the obtained results are compared against experimental and linearized analytical results in order to analyse/measure the low/high fidelity of the model. The CFD numerical model is based on the Reynolds averaged Navier-Stokes (RANS) equation and continuity equation whilst, the linearized analytical model and its solutions are based on velocity potential flow theory. The floating structure is modelled as box-type structure over flat bottom with finite width and draft. The numerical simulation is performed using the open source CFD toolkit, OpenFOAM, with volume of fluid (VOF) method whilst, the linearized analytical solution is based on eigenfunction expansion method. In order to analyse the effect of waves on the floating structure, the results of the vertical motion of the floating structure due to incoming head waves have been compared against the experimental results (Rodriguez and Spinneken, 2016) and analytical solutions in 2D cases. Further, the results of other RAOs and forces obtained from CFD are compared with numerical results available in the literature. It is observed that the CFD results are in good agreement with the experimental data and linear analytical model results, demonstrating reliability and high fidelity of the model.

2. CFD model formulation and description

The Computational Fluid Dynamics (CFD) software used for the presented study is the open source CFD toolkit, OpenFOAM (Open Source Field Operation and Manipulation). OpenFOAM has an extensive range of features to solve complex fluid flows and a wide variety of applications including offshore and coastal engineering problems. The solver has been elaborately discussed by Jasak (1997, 2009).

For this case study, the OpenFOAM release version 2.4.0 was used together with waves2Foam utility to run the simulations. The version 2.4.0 is a stable version of OpenFOAM which has been in use for a long time and is still being used by a large number of research groups. Although updated versions provide more utilities in some cases, the used version was sufficient for the presented case studies. For waves, the library waves2Foam was used to generate and absorb free surface water waves (Jacobsen et al., 2012). The method applies the relaxation zone technique (active sponge layers) and supports a large number of wave theories, and the relaxation zones can be of arbitrary shapes. For the present study, Stokes second order waves were used. The main solver is waveDyMFoam, which is based on the native solver interDyMFoam and is described as a fully viscous solver for two incompressible and immiscible fluids. To simulate the motion of the box because of incoming waves, the OpenFOAM built-in mesh morphing technique with six degrees of freedom of motion (sixDOFRigidBodyMotion) solver is applied. Mesh morphing allows deformation of the mesh or the cells to

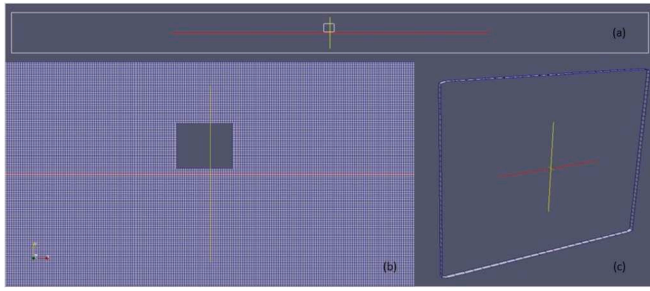


Fig. 1. General Mesh assembly for the 2D box case with 3 degrees of freedom.

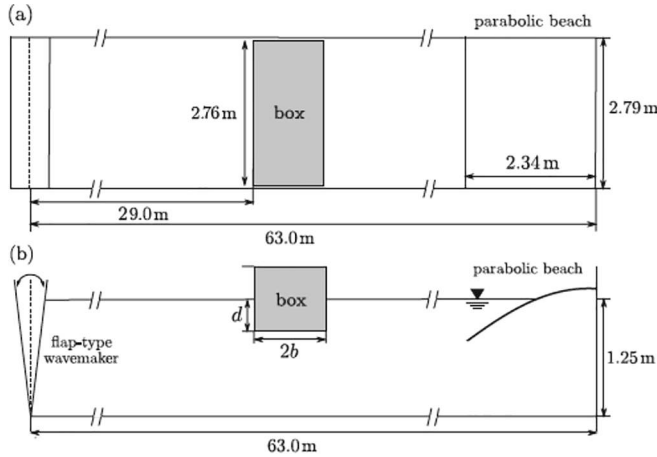


Fig. 2. Schematic of the wave flume setup: (a) plan view and (b) side elevation, Rodriguez and Spinneken (2016).

accommodate the motion of the moving body. The morphing area was defined in a manner that it would be enough to support the mesh deformation, and would cause minimum distortion to the incoming waves. The simulations were run with three outer correctors to have well resolved motion prediction.

2.1. CFD mathematical model

The governing equations for OpenFOAM are the Navier-Stokes equation and continuity equation for an incompressible laminar flow of a Newtonian fluid. In vector form, the Navier-Stokes equation is given by

$$\rho \left(\frac{\partial \mathbf{v}}{\partial t} + \mathbf{v} \cdot \nabla \mathbf{v} \right) = -\nabla p + \mu \nabla^2 \mathbf{v} + \rho \mathbf{g}, \quad (1)$$

where \mathbf{v} is the velocity, p is the pressure, μ is the dynamic viscosity, \mathbf{g} is acceleration due to gravity, and ∇^2 is the Laplace operator. Further, the continuity equation is of the form

$$\nabla \cdot \mathbf{v} = 0. \quad (2)$$

The solver follows Cartesian coordinate system and the volume of fluid method to track the free surface elevation. This volume of fluid method determines the fraction of each fluid that exists in each cell. The equation for the volume fraction is obtained as

$$\frac{\partial \alpha}{\partial t} + \nabla \cdot (\alpha \mathbf{U}) = 0, \quad (3)$$

where \mathbf{U} is the velocity field, α is the volume fraction of water in the cell and varies from 0 to 1, full of air to full of water, respectively. The governing equation is initially discretized using Finite Volume Method (FVM), and pressure velocity coupling is with PISO algorithm.

OpenFOAM offers both SST-K-omega and K-epsilon turbulence models. However, for the presented 2 dimensional (2D) studies, the flow was considered laminar and no turbulence model has been used. This was done to simplify the study, since presence of turbulence model in low wave frequency wave tend to show higher dissipation of waves (Devolder et al., 2017).

2.2. Meshing

Regarding the meshing, OpenFOAM can solve both structured and unstructured meshes. For the presented simulation cases, blockMesh utility was used to generate a structured outer domain with hexahedral mesh. A uniform mesh resolution was applied in the 2 dimensional block mesh with cell size of 0.02 m in wave propagation direction (x-axis) and cell size of 0.01 m in vertical direction (y-axis). The box was integrated into the block using snappyHexMesh utility.

No further refinement was done in the block and near the box. Although the mesh resolution in vertical direction was not enough to provide 6 cells per wave height for all cases, it was enough the capture the heaving motion of the box with acceptable accuracy. Naturally, the prediction results improve with improved mesh resolution; however, considering the large number of simulation cases, a mesh with higher resolution was avoided (see Fig. 1).

2.3. Case setup

The numerical setup was done following the experimental setup described by Rodriguez and Spinneken (2016). All the experiments reported by Rodriguez and Spinneken were performed in the Long Wave Flume of Hydrodynamics Laboratory of Imperial College London. The wave flume is 63 m long, 2.79 m in width and has a height of 1.25 m. Flap type wave makers were used for the study. The experimental setup intended to produce almost two-dimensional flow conditions. For this purpose the width of the rectangular box was chosen to be 2.76 m, leaving only a very small gap of 0.015 m to either of the flume's side walls. A schematic diagram of the experimental setup is shown in Fig. 2. The base experimental cases were performed for steepness (A_{ik}) 0.05 and 0.1, and kb value ranging from 0.2 to 1.2, with interval of 0.1. Here, k is the wave number and b is half of the length of the box.

Following the experimental setup, the numerical setup was produced to replicate a 2D wave flume with 31.5 m length and 1.25 m water depth. The flume length was reduced to ensure less dissipation and also to save computational time. For initial validation study, a rectangular floating box with 0.5 m \times 0.5 m \times 0.01 m dimensions (length \times height \times width) and a draft of 0.25 m was used with heave free motion. Although the simulations were performed in 2D, a width is necessary since OpenFOAM needs a 3D structure to simulate and it is turned into 2D by specifying side boundaries as empty. Thus, the width of 0.01 m has no effect on the simulation. Later, a box with 0.5 m \times 0.4 m \times 0.01 m dimensions, and a draft of 0.2 m was used for simulation with 3DoF (Heave, Pitch and Surge). The box with a lower draft was used for later cases for better pitch stability. The chosen Cartesian coordinates, x-axis is parallel to the flume length and y-axis is parallel to the flume height. The origin in x-axis and y-axis are located in the centre of the domain.

2.4. Computational resource

The simulations were performed in three computers with the configuration of Intel(R) Core i7 CPU with 8 cores, clock speed 3.60 GHz and 16 GB of physical memory. The simulations were performed in Ubuntu operating system with OpenFOAM version 2.4.0. The dynamic time step size was set following the bounding Courant-Freidrichs-Lewy (CFL) number of 0.25. The length of the simulation time was decided based on the wave length, to ensure stable sinusoidal output. On an average, each case took roughly 50 h to simulate.

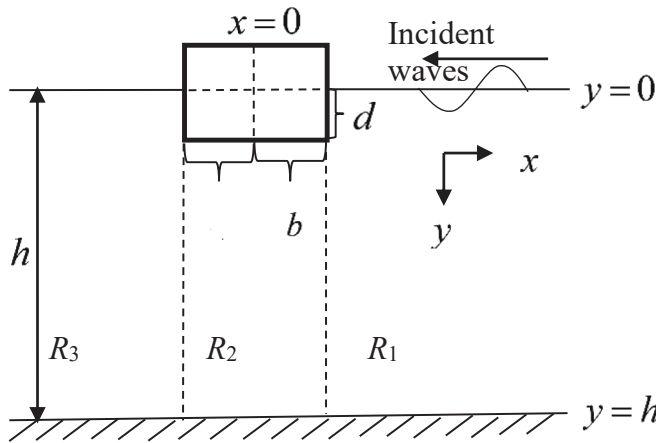


Fig. 3. Schematic diagram for analytical study of wave radiation by a box-type floating structure.

Table 1
Grid dependency analysis for the 2D heaving box.

Heave RAO				
Wave length	λ (m)	3.39	1.96	
Wave height	H (m)	0.063	0.031	
Output values	ϕ_1 (fine)	1.430	0.51	
	ϕ_2 (mid)	1.3300	0.4300	
	ϕ_3 (coarse)	1.2200	0.2900	
Refinement ratio	$r_{12} = h_2/h_1$	2.0000	2.0000	
	$r_{32} = h_3/h_2$	2.0000	2.0000	
Difference of estimation	$\epsilon_{21} = \phi_2 - \phi_1$	-0.1000	-0.0800	
	$\epsilon_{32} = \phi_3 - \phi_2$	-0.1100	-0.1400	
Convergence	$\epsilon_{21/\epsilon_{32}}$	0.9091	0.5714	

Table 2
Simulation cases for the 2D heaving box for validation study.

kb	Aik	H (m)	T (s)	λ (m)
0.3	0.05	0.083	1.92	5.24
0.4	0.05	0.063	1.62	3.93
0.5	0.05	0.050	1.43	3.14
0.6	0.05	0.042	1.30	2.62
0.7	0.05	0.036	1.20	2.24
0.8	0.05	0.031	1.12	1.96
1	0.05	0.025	1.00	1.57
0.4	0.1	0.125	1.62	3.93
0.5	0.1	0.100	1.43	3.14
0.6	0.1	0.083	1.30	2.62
0.7	0.1	0.071	1.20	2.24
0.8	0.1	0.063	1.12	1.96
1	0.1	0.050	1.00	1.57
1.2	0.1	0.042	0.92	1.31

3. Analytical model formulation and linearized solution

The mathematical model of the physical problem is considered in three-dimensional Cartesian coordinate system (x, y, z) with $x - z$ being in the horizontal plane that coincides undisturbed water surface and the y -axis being in the vertical downward positive direction. The wave radiation due to the heave, sway, and roll motions of a rectangular structure floating on the free surface of width $2b$, draft d , and infinitely long in the z -direction. The origin o is assumed to be the middle point of the rectangular structure (as in Fig. 3). Hence, the whole fluid domain is divided into three-regions as defined by: $(b < x < \infty, 0 < y < h)$,

$(-b < x < b, d < y < h)$ and $(-b < x < -\infty, 0 < y < h)$ are referred as R_1 , R_2 , and R_3 respectively.

The water is assumed to be inviscid, incompressible and flow is irrotational and simple harmonic in time with angular frequency ω and also in the z -direction. Thus, there exists a velocity potential $\phi(x, y, z, t) = \text{Re}\{\phi(x, y, z)\exp(-i\omega t)\}$, where Re denotes the real part of the complex expression and $\phi(x, y, z)$ denotes the spatial velocity potential.

The potential $\phi(x, y, z)$ may be decomposed into the incident wave potential, the diffracted potential (due to the stationarity of the structure) and the radiated potential (due to the heave, sway, and roll motions of the floating structure) are denoted by ϕ_I , ϕ_D , and ϕ_R respectively. So the total potential $\phi(x, y, z)$ can be expressed as (see Zheng et al., 2006)

$$\phi = \phi_I + \phi_D + \sum_{S=1}^3 \phi_R^{(S)}, \quad (4)$$

where $S = 1, 2$, and 3 stand for heave, sway, and roll motions, respectively.

Assuming that a progressive wave interacts with a floating rectangular structure making an oblique angle θ with x -axis and angular frequency ω , thus, the spatial incident velocity potential is of the form $\phi_I(x, y, z) = \phi_I(x, y)e^{i\gamma z}$, $\gamma = k_0 \sin \theta$ is the z -component of the wave number k_0 associated with the incident waves. Therefore, the incident wave potential of linear waves propagating to the negative x -direction is given by

$$\phi_I = \frac{igI}{\omega} \frac{\cosh k_0(h-y)}{\cosh k_0 h} e^{-ipx}, \quad (5)$$

where g is acceleration due to gravity, I is the incident wave amplitude with the dimension of length and is taken as 1 without loss of any generality in the numerical computation and $p = k_0 \cos \theta$ is the x -component of the wave number k_0 associated with the incident wave and k_0 satisfy the gravity wave dispersion relation as given by

$$\omega^2 = gk_0 \tanh(k_0 h). \quad (6)$$

Assuming that the motions of the structure are small and the oscillations vary sinusoidally in the z -direction (This assumptions have been used previously by many researchers; Losada et al., 1992; Sannasiraj et al., 1995; Abul-Azm and Williams, 1997; Abul-Azm and Gesraha, 2000; Zheng et al., 2006) and the amplitude of motion mode S of the floating structure is denoted by $I_R^{(S)}$. Thus, the radiated potential $\phi_R^{(S)}$ can be expressed as

$$\phi_R^{(S)}(x, y, z) = -i\omega I_R^{(S)} \phi_R^{(S)}(x, y) e^{i\gamma z}, \quad (7)$$

where $\phi_R^{(S)}$ is the spatial velocity potential independent of z which satisfies the reduced wave equation

$$(\nabla_{xy}^2 - \gamma^2) \phi_R^{(S)} = 0 \text{ in the fluid domain}, \quad (8)$$

where $\nabla_{xy}^2 = \partial^2/\partial x^2 + \partial^2/\partial y^2$ is the two-dimensional Laplacian operator.

Combining the kinematic and dynamic boundary conditions, the linearized boundary condition at the mean free surface is obtained as

$$\frac{\partial \phi_R^{(S)}}{\partial y} + K \phi_R^{(S)} = 0 \text{ on } y = 0 \text{ for } R_1 \text{ and } R_3, \quad (9)$$

where $K = \omega^2/g$.

The no flow conditions at the rigid bottom boundary are given by

$$\frac{\partial \phi_R^{(S)}}{\partial y} = 0 \text{ on } y = h \text{ for } R_1, R_2 \text{ and } R_3 \quad (10a)$$

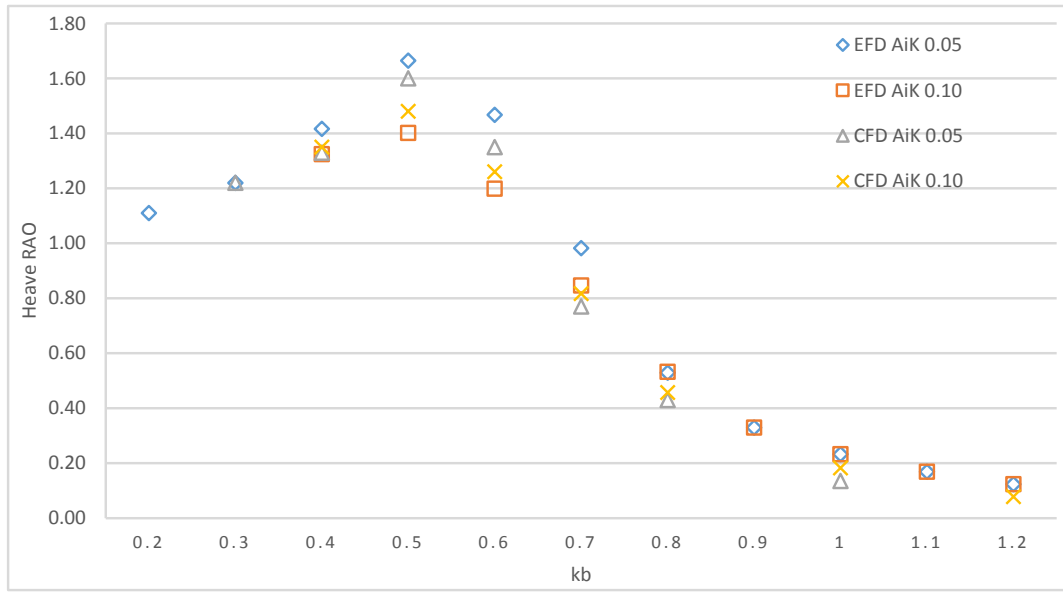


Fig. 4. Comparison between CFD and EFD results for the heave RAO at two different wave steepness.

Table 3

Convergence study of wave forces of heave, sway, and roll motions for $d = 0.5h$, $l = 0.417h$, $h = 0.75h$, and $\theta = 60^\circ$.

No. of terms	Wave forces		
N	F_1 (Vertical force)	F_2 (Horizontal force)	F_3 (Torque)
5	0.6556	0.7043	0.2649
10	0.6544	0.7068	0.2676
15	0.6538	0.7076	0.2685
20	0.6532	0.7080	0.2691
25	0.6531	0.7082	0.2693
30	0.6530	0.7084	0.2695
31	0.6530	0.7084	0.2695

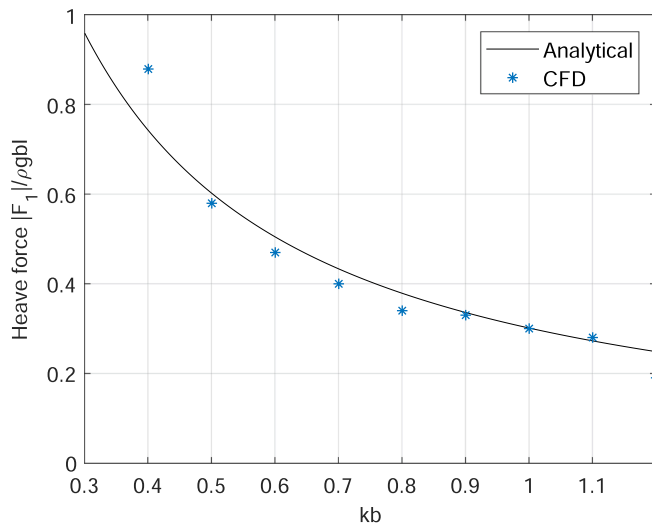


Fig. 5. Comparison between the analytical and CFD model of vertical wave force on the box-type floating structure.

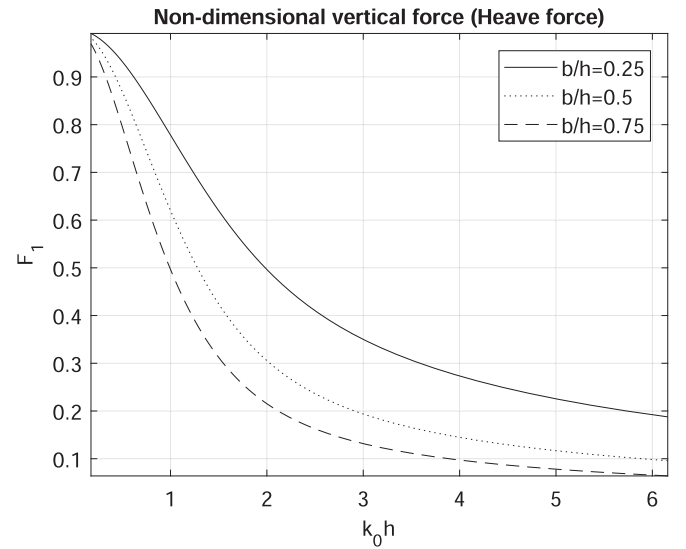


Fig. 6. Effect of structural width on non-dimensional vertical wave force F_1 with $d/h = 0.5$.

$$\frac{\partial \varphi_R^{(S)}}{\partial x} = 0 \text{ on } x = b \quad (10b)$$

The non-homogeneous boundary condition due to the heave, sway, and roll motions of the floating rectangular structure is given by

$$\frac{\partial \varphi_R^{(S)}}{\partial y} = \delta_{1,S} - (x - x_0)\delta_{3,S} \text{ on } -b \leq x \leq b, y = d. \quad (11)$$

The conditions on the rigid structural boundary are described as

$$\frac{\partial \varphi_R^{(S)}}{\partial x} = \delta_{2,S} + (y - y_0)\delta_{3,S} \text{ at } x = \pm b, \text{ and } 0 < y < d, \quad (12)$$

where (x_0, y_0) is the centre of rotation for roll motion and δ = Kronecker delta function as defined by

$$\delta_{j,S} = \begin{cases} 0 & \text{for } j \neq S, \\ 1 & \text{for } j = S. \end{cases} \quad (13)$$

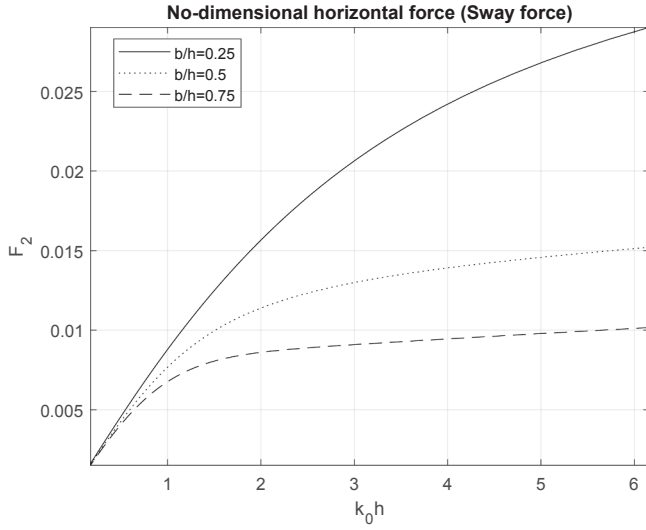


Fig. 7. Effect of structural width on non-dimensional horizontal wave force F_2 $d/h = 0.5$.

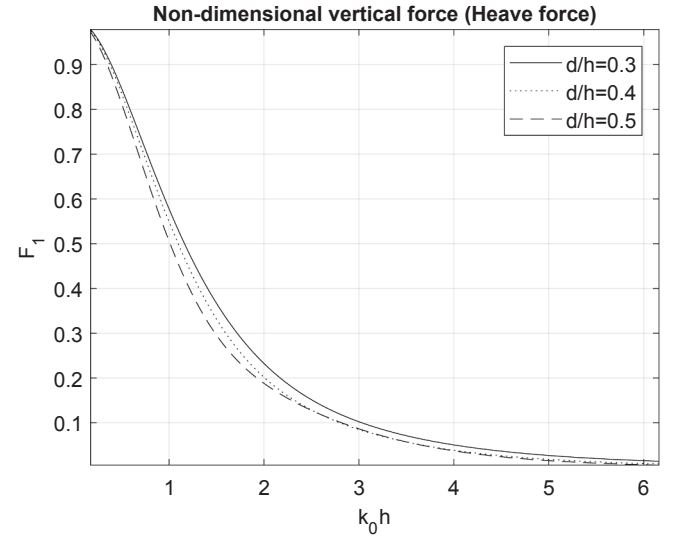


Fig. 9. Variation of draft on non-dimensional of vertical wave force F_1 with $h/l = 1.2$.

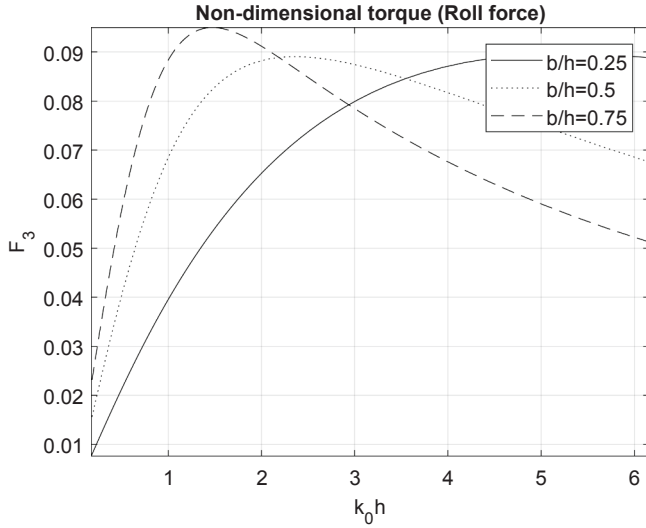


Fig. 8. Effect of width on non-dimensional torque F_3 with $d/h = 0.5$.

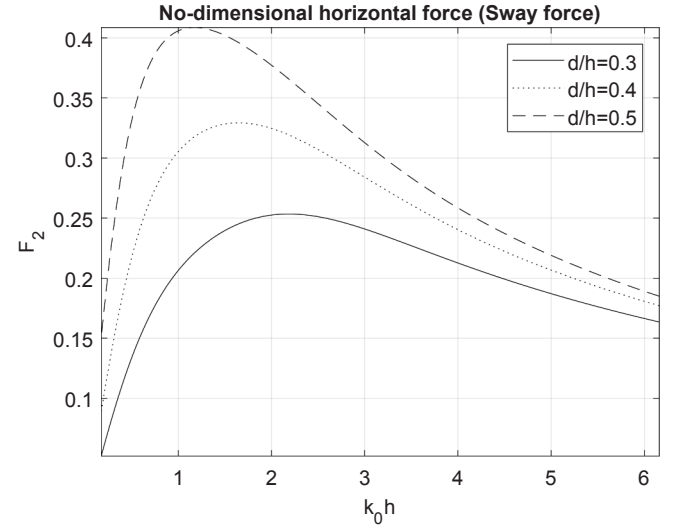


Fig. 10. Variation of draft on non-dimensional of horizontal force F_2 with $h/l = 1.2$.

Further, the radiation condition is assumed to take of the form

$$\lim_{x \rightarrow \mp \infty} \left[\frac{\partial \varphi_R^{(S)}}{\partial x} \pm i p \varphi_R^{(S)} \right] = 0. \quad (14)$$

The next Section will obtain the analytical expressions for radiation potentials in each region and their solutions by satisfying the governing equations along with the relevant boundary conditions.

Using the method of separation of variables in three regions R_1 , R_2 , and R_3 , the radiated potentials $\varphi_R^{(S)}$ satisfying (8) along with the relevant boundary conditions (9–14) are expanded as (as in Islam et al., 2018)

$$\varphi_{R1}^{(S)} = A_{10}^{(S)} e^{ip_0(x-b)} u_0(y) + \sum_{n=1}^{\infty} A_{1n}^{(S)} e^{p_n(x-b)} u_n(y), \quad (15)$$

$$\begin{aligned} \varphi_{R2}^{(S)} = & \frac{-\cosh \alpha_0(h-y)}{\alpha_0 \sinh \alpha_0(h-d)} \{ \delta_{1,S} - (x-x_0) \delta_{3,S} \} \\ & + \sum_{n=0}^{\infty} [A_{2n}^{(S)} e^{-\alpha_n(x-b)} + B_{2n}^{(S)} e^{\alpha_n(x+b)}] v_n(y), \end{aligned} \quad (16)$$

$$\varphi_{R3}^{(S)} = A_{30}^{(S)} e^{-i k_0(x+b)} w_0(y) + \sum_{n=1}^{\infty} A_{3n}^{(S)} e^{\lambda_n(x+b)} w_n(y), \quad (17)$$

where the eigenfunctions $u_n(y)$'s, $v_n(y)$'s and $w_n(y)$'s in Eqs. (15)–(17) are obtained as

$$u_0(y) = \frac{\cosh k_0(h_1 - y)}{\cosh k_0 h_1}, \quad u_n(y) = \frac{\cos k_n(h_1 - y)}{\cos k_n h_1}, \quad (18)$$

$$v_n(y) = \cos \beta_n(h_2 - y), \quad (19)$$

$$w_0(y) = \frac{\cosh \mu_0(h_2 - y)}{\cosh \mu_0 h_2}, \quad \text{and } w_n(y) = \frac{\cos \mu_n(h_2 - y)}{\cos \mu_n h_2}, \quad (20)$$

with the eigenvalues k_0 is same as defined in Eq. (6) and $k_n = i k_n$, p_n 's, α_n 's, β_n 's, and μ_n 's are satisfy the following dispersion relations (as in Bhattacharjee and Guedes Soares, 2011)

$$\omega^2 = -g k_n \tan(k_n h_1), \quad (21)$$

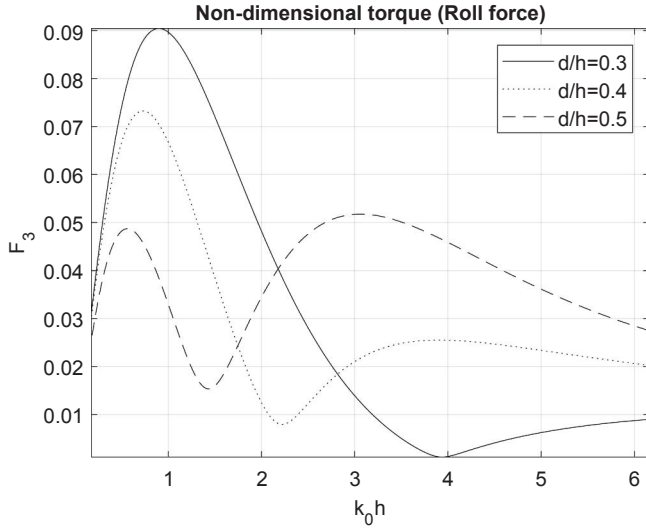


Fig. 11. Variation of draft on non-dimensional of torque F_3 with $h/l = 1.2$.

Table 4
Simulation cases for the 2D box with 3DoF for comparison study.

kb	Aik	H (m)	T (s)	λ (m)
0.3	0.05	0.083	1.92	5.24
0.5	0.05	0.050	1.43	3.14
0.6	0.05	0.042	1.30	2.62
0.7	0.05	0.036	1.20	2.24
0.4	0.1	0.125	1.62	3.93
0.5	0.1	0.100	1.43	3.14
0.6	0.1	0.083	1.30	2.62
0.7	0.1	0.071	1.20	2.24
0.8	0.1	0.063	1.12	1.96
0.9	0.1	0.056	1.06	1.75
1	0.1	0.050	1.00	1.57
1.1	0.1	0.045	0.96	1.43
1.2	0.1	0.042	0.92	1.31

$$p_n = \begin{cases} k_0 \cos \theta & \text{for } n = 0, \\ \sqrt{k_n^2 + \gamma^2} & \text{for } n = 1, 2, \dots, \end{cases} \quad (22)$$

$$\alpha_n = \begin{cases} k_0 \sin \theta & \text{for } n = 0, \\ \sqrt{\beta_n^2 + \gamma^2} & \text{for } n = 1, 2, \dots, \end{cases} \quad (23)$$

$$\beta_n = \frac{n\pi}{(h_2 - d)} \text{ for } n = 0, 1, 2, \dots, \quad (24)$$

$$\omega^2 = g\mu_0 \tanh(\mu_0 h_2) \text{ for } n = 0 \text{ and } \omega^2 = -g\mu_n \tan(\mu_n h_2) \text{ for } n = 1, 2, \dots \quad (25)$$

$$\lambda_n = \begin{cases} \mu_0 \cos \theta, & \text{for } n = 0, \\ \sqrt{\mu_n^2 + \gamma^2}, & \text{for } n = 1, 2, \dots \end{cases} \quad (26)$$

Further, the eigenfunction $u_n(y)$'s, $v_n(y)$'s and $w_n(y)$'s are orthogonal with respect to their own intervals as defined by

$$\langle u_n, u_m \rangle = \int_0^{h_1} u_n(y) u_m(y) dy = \delta_{mn} U_n, \quad (27)$$

$$\langle v_n, v_m \rangle = \int_d^{h_2} v_n(y) v_m(y) dy = \delta_{mn} V_n, \quad (28)$$

$$\langle w_n, w_m \rangle = \int_0^{h_2} w_n(y) w_m(y) dy = \delta_{mn} W_n, \quad (29)$$

where

$$U_n = \begin{cases} \frac{1}{2 \cosh^2 k_n h_1} \left(h_1 + \frac{\sinh 2k_n h_1}{2k_n} \right), & \text{for } n = 0, \\ \frac{1}{2 \cos^2 k_n h_1} \left(h_1 + \frac{\sin 2k_n h_1}{2k_n} \right), & \text{for } n = 1, 2, \dots, \end{cases}$$

$$V_n = \begin{cases} (h_2 - d), & n = 0 \\ \frac{1}{2}(h_2 - d), & n = 1, 2, 3, \dots, \end{cases}$$

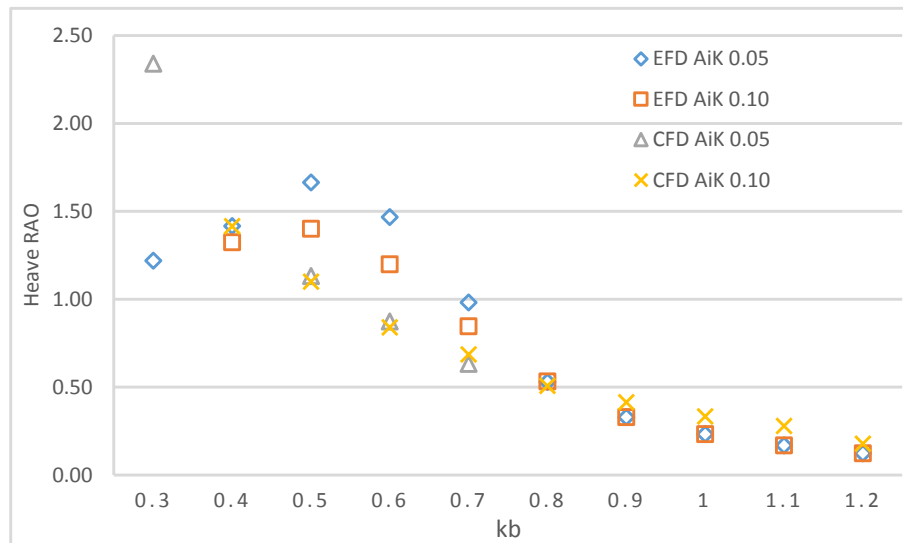


Fig. 12. Comparison between EFD and CFD Heave RAO results, where CFD results are for a box with lower draft (0.2 m).

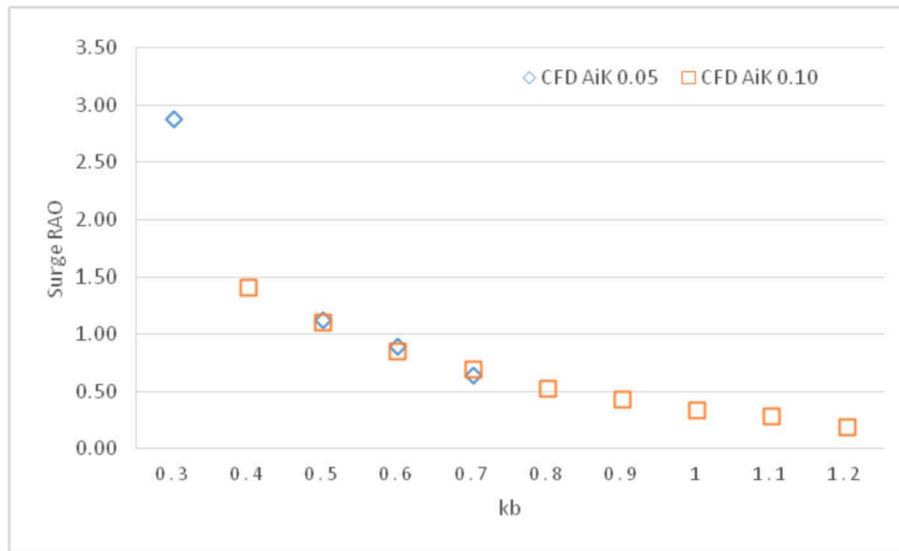


Fig. 13. CFD simulation results for the Surge RAO at two different wave steepness.



Fig. 14. CFD simulation results for the Pitch RAO at two different wave steepness.

$$W_n = \begin{cases} \frac{1}{2 \cosh^2 \mu_n h_2} \left(h_2 + \frac{\sinh 2\mu_n h_2}{2\mu_n} \right), & \text{for } n = 0, \\ \frac{1}{2 \cos^2 \mu_n h_2} \left(h_2 + \frac{\sin 2\mu_n h_2}{2\mu_n} \right), & \text{for } n = 1, 2, \dots, \end{cases}$$

with δ_{mn} is being same as defined in Eq. (12).

Now, substituting the velocity potentials (15–17) into the continuity of velocity and pressure condition across the vertical interfaces at $x = \pm b$.

Continuity of velocity at vertical interface $x = l$ is given by

$$\frac{\partial \varphi_{R1}^{(S)}}{\partial x} = \begin{cases} \delta_{2,S} + (y - y_0) \delta_{3,S} & \text{for } 0 < y < d, \\ \frac{\partial \varphi_{R2}^{(S)}}{\partial x} & \text{for } d < y < h_2, \\ 0 & \text{for } h_2 < y < h_1. \end{cases} \quad (30a)$$

Continuity of velocity at vertical interface $x = -l$ is given by

$$\frac{\partial \varphi_{R3}^{(S)}}{\partial x} = \begin{cases} \delta_{2,S} + (y - y_0) \delta_{3,S} & \text{for } 0 < y < d, \\ \frac{\partial \varphi_{R2}^{(S)}}{\partial x} & \text{for } d < y < h_2. \end{cases} \quad (30b)$$

Again, the continuity of pressure at the vertical interfaces $x = \pm l$ are given by

$$\varphi_{R1}^{(S)} = \varphi_{R2}^{(S)} \quad \text{at } x = l \text{ for } d < y < h_2 \quad (31a)$$

$$\varphi_{R2}^{(S)} = \varphi_{R3}^{(S)} \quad \text{at } x = -l \text{ for } d < y < h_2 \quad (31b)$$

and using the orthogonal conditions (25–27), a linear system of equations $4(N+1)$ is obtained to solve for $4(N+1)$ number of unknown coefficients $A_{1n}^{(S)}$'s, $A_{2n}^{(S)}$'s, $A_{3n}^{(S)}$'s, and $B_{2n}^{(S)}$'s for motion mode S as:

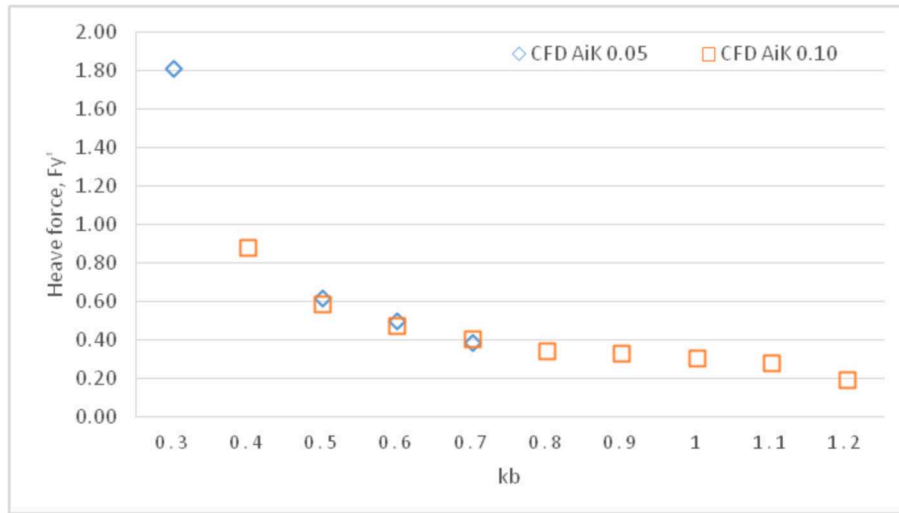


Fig. 15. CFD simulation result for the non-dimensional heave force at two different wave steepness.

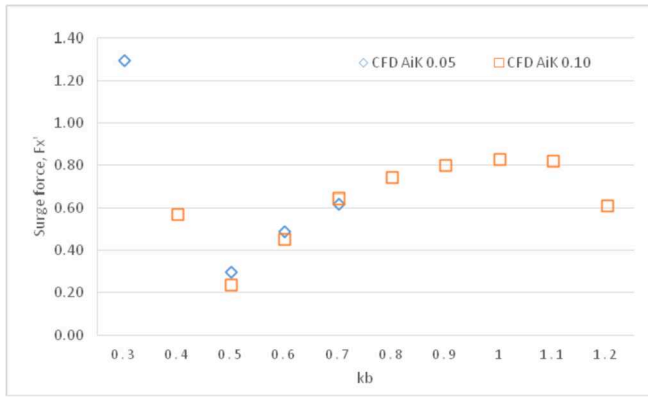


Fig. 16. CFD simulation result for the non-dimensional surge force at two different wave steepness.

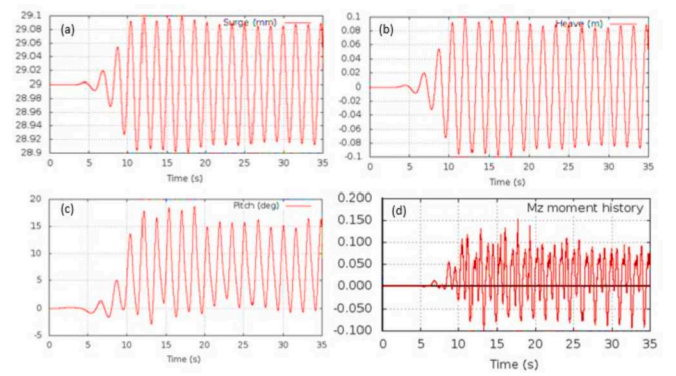


Fig. 18. Time history for the surge (a), heave (b), pitch motion (c) and pitch moment (d) for the moving box due to incoming waves, at wave period 1.62 s.

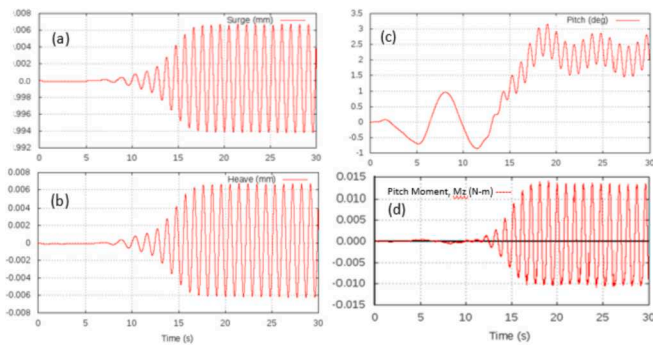


Fig. 17. Time history for the surge (a), heave (b), pitch motion (c) and pitch moment (d) for the moving box due to incoming waves, at wave period 0.96 s.

$$\begin{aligned}
 & ip_0 A_{10}^{(S)} U_0 - \sum_{n=0}^N \alpha_n \left(-A_{2n}^{(S)} + B_{2n}^{(S)} e^{2\alpha_n l} \right) \int_d^{h_2} u_0(y) v_n(y) dy \\
 &= \int_0^d \left[\left\{ \delta_{2,S} + (y - y_0) \delta_{3,S} \right\} + \delta_{3,S} \frac{\cosh \alpha_0 (h_2 - y)}{\alpha_0 \sinh \alpha_0 (h_2 - d)} \right] u_0(y) dy \quad \text{for } m = 0,
 \end{aligned}
 \tag{32a}$$

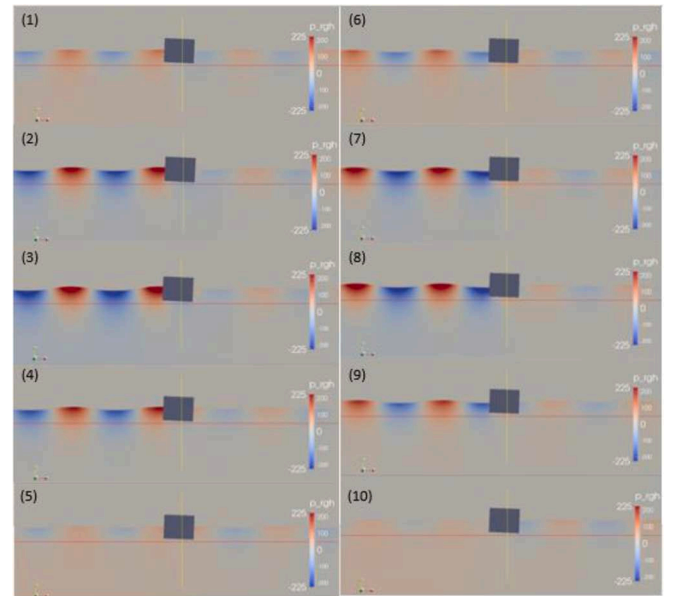


Fig. 19. Hydrodynamic pressure distribution in the simulation domain during wave encounter by the 2D box with 3DOF, for wave period 0.96 s and wave height 0.045 m.

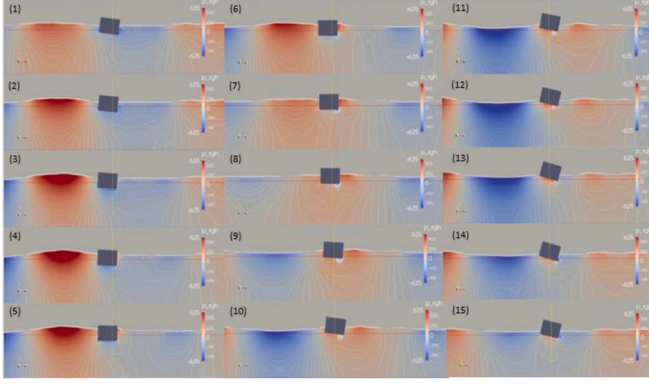


Fig. 20. Hydrodynamic pressure distribution in the simulation domain during wave encounter by the 2D box with 3DOF, for wave period 1.62 s and wave height 0.125 m.

$$\begin{aligned}
 & -p_m A_{1m}^{(S)} U_m - \sum_{n=0}^N \alpha_n (-A_{2n}^{(S)} + B_{2n}^{(S)} e^{2\alpha_n l}) \int_d^{h_2} u_m(y) v_n(y) dy \\
 & = \int_0^d \left[\left\{ \delta_{2,S} + (y - y_0) \delta_{3,S} \right\} + \delta_{3,S} \frac{\cosh \alpha_0 (h_2 - y)}{\alpha_0 \sinh \alpha_0 (h_2 - d)} \right] u_m(y) dy \quad \text{for } m = 1, 2, \dots, N,
 \end{aligned} \quad (32b)$$

$$\begin{aligned}
 & -i \lambda_0 A_{30}^{(S)} W_0 - \sum_{n=0}^N \alpha_n (-A_{2n}^{(S)} e^{2\alpha_n l} + B_{2n}^{(S)}) \int_0^{h_2} w_0(y) v_n(y) dy \\
 & = \int_0^d \left\{ \delta_{2,S} + (y - y_0) \delta_{3,S} \right\} w_0(y) dy
 \end{aligned} \quad (33a)$$

$$\begin{aligned}
 & + \frac{\delta_{3,S}}{\alpha_0 \sinh \alpha_0 (h_2 - d)} \int_d^{h_2} \cosh[\alpha_0 (h_2 - y)] w_0(y) dy, \text{ for } m = 0, \\
 & \lambda_m A_{3m}^{(S)} W_m - \sum_{n=0}^N \alpha_n (-A_{2n}^{(S)} e^{2\alpha_n l} + B_{2n}^{(S)}) \int_0^{h_2} w_m(y) v_n(y) dy \\
 & = \int_0^d \left\{ \delta_{2,S} + (y - y_0) \delta_{3,S} \right\} w_m(y) dy \\
 & + \frac{\delta_{3,S}}{\alpha_0 \sinh \alpha_0 (h_2 - d)} \int_d^{h_2} \cosh[\alpha_0 (h_2 - y)] w_m(y) dy, m = 1, 2, \dots, N.
 \end{aligned} \quad (33b)$$

$$\begin{aligned}
 & \sum_{n=0}^N A_{1n}^{(S)} \int_d^{h_2} u_n(y) v_m(y) dy - (A_{2m}^{(S)} + B_{2m}^{(S)} e^{2\alpha_m l}) V_m \\
 & = \left\{ \delta_{1,S} - (l - x_0) \delta_{3,S} \right\} \int_d^{h_2} \frac{-\cosh \alpha_0 (h_2 - y)}{\alpha_0 \sinh \alpha_0 (h_2 - d)} v_m(y) dy, \text{ for } m = 0, 1, 2, \dots, N.
 \end{aligned} \quad (34)$$

$$\begin{aligned}
 & \sum_{n=0}^N A_{3n}^{(S)} \int_d^{h_2} w_n(y) v_m(y) dy - (A_{2m}^{(S)} e^{2\alpha_m l} + B_{2m}^{(S)}) V_m \\
 & = \left\{ \delta_{1,S} + (l + x_0) \delta_{3,S} \right\} \int_d^{h_2} \frac{-\cosh \alpha_0 (h_2 - y)}{\alpha_0 \sinh \alpha_0 (h_2 - d)} v_m(y) dy, m = 0, 1, 2, \dots, N.
 \end{aligned} \quad (35)$$

In order to solve the system of linear eqs (32)–(35) through the numerical methods (Matlab code), the infinite series sums are truncated

after finite number of N -terms present in Eqs. (15)–(17). Once the unknown coefficients $A_{1n}^{(S)}$'s, $A_{2n}^{(S)}$'s, $A_{3n}^{(S)}$'s and $B_{2n}^{(S)}$'s for $n = 0, 1, 2, \dots$ are determined, then the full solution will be obtained in terms of radiated potentials.

As the floating structure is assumed to be infinite in the z -direction and also the potential is periodic in the z -direction, hence only the wave forces acting on a cross-section perpendicular to the z -axis to be considered. Thus, the wave forces in terms of incident and radiated potentials can be expressed as (see Zheng et al., 2006; Ngina et al., 2015)

$$F_{ej} = i \rho \omega \left[\int_{S_b} \varphi_I(x, y) n_j ds - \int_{S_b} \varphi_R^j(x, y) \frac{\partial \varphi_I}{\partial n} ds \right] \quad \text{for } j = 1, 2 \quad (36)$$

where S_b denotes the wetted surface in xy plane and n_j is the inward normal to the floating structure in the xy -plane with $n_1 = n_y$, $n_2 = n_x$ and $n_3 = (y - y_0)n_x - (x - x_0)n_y$, n_x and n_y are the components of unit normal to the floating structure.

The non-dimensional wave forces of heave (for $j = 1$, vertical force), sway (for $j = 2$, horizontal force), and roll (for $j = 3$, torque) motions are defined by

$$F_j = \begin{cases} \frac{|F_{ej}|}{(2\rho g b l)} & \text{for } j = 1, 2, \\ \frac{|F_{ej}|}{(2\rho g b^2 l)} & \text{for } j = 3. \end{cases} \quad (37)$$

In the next section, the numerical CFD model of vertical force (heave) will be validated with the experimental model results and then also compared with linearized analytical model results for analyse the level of accuracy as physically, vertical (heave) motion is of primary importance for the hydrodynamic analysis of a floating structure for designing wave energy converters.

4. Results and discussion

A free floating box, under wave encounter, would experience principally three types of forces, deflection, diffraction and radiation. The deflection and diffraction forces are caused by the interaction of the incident waves with the box. Whereas, the radiation forces come from the radiated waves generated because of the motion of the box. Generally, in CFD studies, the body force is derived from the integrated pressure on the floating body during the encounter with the waves, and motions are measured by tracking the centre of gravity location.

In this study, instead of 3D, a 2D box was simulated to ensure proper validation with the Rodriguez and Spinneken (2016) box case, since the experimental setup was done in a manner to resemble a 2D case. Furthermore, considering the large number of simulation cases, 2D significantly reduces the computational time required comparing to 3D cases.

Boxes with two different drafts were simulated, one for the validation study with just heave free motion and the other for studying the 3 degrees of freedom (DoF) cases with heave, surge and pitch free motion. This was done because the box with even length and draft ($b = d$) has lower pitch stability. Since mooring was not used in the simulations, the easiest solution to make the box pitch stable was to make the length longer than the height ($b > d$). Understandably, such a configuration is not good for a wave energy converters (WEC), since they have lower heave RAO. However, the purpose of this paper is not to find the optimum configuration for a box type WEC device, rather to compare the CFD results with analytical model to understand the level of fidelity of the used analytical model.

To non-dimensionalise the heave, surge and pitch RAOs (Response Amplitude Operator), and the surging and heaving force, following equations were used.

$$\left. \begin{aligned} \text{Heave RAO} &= \zeta_H/H_I, \\ \text{Surge RAO} &= \zeta_S/H_I, \\ \text{Pitch RAO} &= (\theta^*\lambda)/(H^*360), \\ F_x^* &= F_x/\rho g d w H_I, \\ F_y^* &= F_y/\rho g d w H_I, \end{aligned} \right\} \quad (38)$$

where ζ_H is the heave, ζ_S is the surge displacement, H_I is the incoming wave height, θ is the total pitch displacement, and λ is the incoming wave length. Further, F_x and F_y are the dimensional surge and heave force respectively, ρ is the water density, g is the gravitational acceleration, b is the half length of the box, d is the draft, and w is the width.

4.1. Validation study

Initially a validation study was performed following the Rodriguez and Spinneken (2016) box case and the CFD simulation results were compared to their experimental results. For validation study, a 2D box with $0.5 \times 0.5 \text{ m}^2$ ($b = 0.25$, $d = 0.25$) dimension was simulated in a numerical tank with length 31.5 m and 1.25 m depth. The long domain was used to ensure enough space for the inlet relaxation zone and smooth propagation of wave to the box. Only heave RAO results are provided from the experimental study for the heaving box. Thus, these are the only results that were compared.

To ensure reliability of the results, a grid convergence study was performed following ITTC (2008) guidelines. Three different mesh resolutions were used, coarse (0.078 million), medium (0.35 million) and fine (1.25 million). In coarse mesh, the cell spacing in x-axis was 0.04 and in y-axis 0.02; for medium mesh the spacing was 0.02 and 0.01; and for fine mesh it was 0.01 and 0.005 in x and y axis respectively. Both the cases that were studied for grid dependency showed monotonous convergence, as shown in Table 1. In the table, ϕ_n is the solution result for the particular grid and h_n is the cell size of mesh n . The results significantly improve with improved mesh resolution. However, considering resource limitation, for rest of all the simulations, the medium mesh resolution was used.

The simulated cases are shown in Table 2 and the simulation results together with experimental fluid dynamics (EFD) results are shown in Fig. 4. As can be seen from Table 2, simulations were performed for two different wave steepness and the CFD results show good agreement with experimental data (Fig. 4). The slight deviation observed between the EFD and CFD data is mostly because of insufficient mesh resolution and the results improve with higher resolution, as shown in the grid dependency study. The results also show that the heave response of the box is not linear for different wave steepness, indicating the importance of using viscous non-linear solvers for studying such structures. Here, k represents the wave number, b is half of the length of the floating box, A_i is the incident wave amplitude and A_{ik} is the wave steepness. H is the wave height, T is the wave period and λ is the wave length.

Fig. 4 also shows that the heaving box shows optimum heave response for a wave length of around 3 m. The experimental results also show that better response is observed for waves with less steepness. However, CFD, at its present resolution, fails to capture that properly except for near optimal performance area. This is mostly because of the mesh resolution. Since, the mesh resolution used for both wave steepness were the same, higher amplitude cases has greater number of cell per wave height, comparing to the low steepness cases. As such, low steepness cases face comparatively higher dissipation during propagation and under predict the estimations.

4.2. Comparison between CFD and analytical model with hydrodynamic effect on 3DOF results

In order to check the computational accuracy, the convergence of the series solutions is demonstrated in Table 3 by computing the values of

hydrodynamic coefficients of heave, sway, and roll motions of the floating structure in two-dimensional case. From Table 1, it is clear that the values of F_j for $j = 1, 2, 3$ are correct up to three decimal places for values of N greater than or equal to 30. Thus, for numerical accuracy, the number of terms N in the radiation velocity potential formulae is restricted to 30 in the computation. On the other hand, it may be noted that as the bottom is flat it is considered that $h_1 = h_3 = h$ and $h_2 = h - d$.

Fig. 5 shows the comparison of CFD against linearized analytical results of non-dimensional vertical wave force acting on the floating box versus kb . It is observed that the CFD result is almost same with analytical model results for almost all values of kb and the vertical force behaviour pattern is similar in nature for both models. However, small deviation between them is observed for higher and lower values of kb which observation is similar as in Islam et al. (2018). These differences can be explained by the full non-linearity solution of the CFD model, while the solution of the analytical model is only of linear. It is also suspected that the viscous effects considered in the CFD model can play an important part in the description of the wave force profile, while these effects are neglected in the analytical approach.

The non-dimensional forces for the heave, sway and roll are shown in Figs. 6–8, respectively. Explicitly, the variation of the non-dimensional vertical wave force F_1 , horizontal wave force F_2 , and torque F_3 for different non-dimensional width b/h of the structure with $d/h = 0.5$ versus $k_0 h$ are plotted. It is observed that the vertical and horizontal wave forces decreases with increase in width of the structure which may be due to the interaction of incident and reflected waves in region 1. This observation is similar as in Zheng et al. (2006) and also same as in Guo et al. (2018) in case of wave diffraction by a floating rectangular structure. On the other hand, the torques increases with increase in the value of width of the structure for smaller value of wave number and its effect becomes opposite in nature for higher values of wave number. However, the horizontal wave force is less than that of vertical wave forces.

Figs. 9–11 plot the variations of the non-dimensional vertical wave force F_1 , horizontal wave force F_2 , and torque F_3 respectively for different non-dimensional draft d/h with $h/l = 1.2$ versus $k_0 h$. It is observed that the non-dimensional vertical wave forces increases with decrease in draft whilst, the horizontal force increases with increase in non-dimensional draft. This is due to the deeper drafts causes more horizontal load on the floating box and smaller load in vertical. These observations are similar in the cases of oblique wave diffraction by a floating structure on a stepped bottom as in Bhattacharjee and Guedes Soares (2011). The peaks are observed in torques for smaller values of wave number and it attends zero for lower value of non-dimensional draft. Further, the observations in vertical force for both width and draft are similar as in Figs. 5 and 8.

4.3. CFD simulation results for floating box with 3 DOF

After validation and comparison study, simulations were performed for the 2D box with 3DoF (heave, surge and pitch), with a different draft ($d = 0.2$). Except the draft, all other domain settings and mesh remained the same. The simulation cases performed for the comparison study are shown in Table 4. For comparison, mostly high wave steepness cases were simulated.

The results for the heave, surge and pitch RAOs are shown in Figs. 12–14, respectively. The heave RAO results show that the shallower draft shows lower heave response for the low wave frequency cases, however shows reduced motion in near resonance cases. Furthermore, the wave steepness has very limited influence on heave response of the box, comparing to the even length and height cases. Nevertheless, the box follows very similar heaving motion pattern as observed in the experimental study.

The surge and pitch RAO results show that the natural frequency for the surge and pitch motion for the box is not the same as that of the heave motion. According to the results, the natural frequency for the

surge and pitch motion stands in the higher wavelength region comparing to the heave response. Furthermore, the results also show minimum variation in the motion response due to difference in incoming wave steepness. The results also indicate that comparing to the heave motion, the surge and pitch response of the box is quite low.

The heave and surge force results are shown in Figs. 15 and 16. The figures well represent the motion response figures. The figures indicate that the heave force increases with the increasing wave period and the so does the surge force. The RAOs are justified by the forces acting on them, as the motions increase with the increasing force acting on them. The pitch moment results have not been shown here since the pitch moment showed a non-sinusoidal response. For proper capturing of the response, and FFT was essential, thus it was avoided.

To further illustrate the results, time history of the surge, heave, pitch motion and pitch moment for the wave period 0.96 s and wave height 0.045 m are shown in Fig. 17. Because of the length of the simulation domain, it takes roughly 10 s for the waves to reach the box. Thus, motion response of the box due to the incoming waves is observed after 10 s. Both, surge and heave motions show sinusoidal response to the incoming waves and the response remains the same over the time period. As for the pitch motion, the time history shows that, before the box encounters the waves, it oscillates in natural pitch frequency. After facing the incoming waves, the box aligns itself to the pitch stable condition, which seems to be at around 2.25° , and oscillates with the incoming waves. The description can be supported by the pitch moment history, which shows stable sinusoidal pitch moment.

To demonstrate the difference in response of the box due to changing wave conditions, time history for the wave period 1.62 s, with wave height of 0.125 m is also shown in Fig. 18. Unlike previous case, longer wave period and greater wave height shows more non-linear behaviour, for both the motions, and the forces and moments.

To demonstrate the wave encounter by the box, the hydrodynamic pressure field gained from the simulations for cases with wave period 0.96 and 1.62 s are shown in Figs. 19 and 20, respectively. The figures show gradual wave encounter by the box. The high and low pressure points indicate the wave crest and trough. Irrespective of the wave condition, the box maintains a slight pitch angle, indicating that the pitch stability is not at zero while encountering waves. For the first case (period 0.96 s), both the wave period and the wave height are small, thus the response motions are also small. As for the second case, due to larger wave period and greater wave height, the motion of the box is more pronounced. The vortices generated below the box are also well visible. The figures show that the box maintains a low pressure below while facing the wave crest and a high pressure while facing the wave trough. This opposite pressure helps dampen the motion of the box while facing the waves.

5. Conclusions

This paper studied the wave radiation due to a moving box-type floating structure due to incoming waves, and compared the vertical force results among the CFD, experimental and linearized analytical model solution results. Further, the simulated results of RAO in CFD are also compared with experimental results available in the literature. The validation and comparison of the numerical wave flume (CFD) for working with a box-type floating structure based on experimental model data and the linearized velocity potential theory results are demonstrated to be successful.

However, the paper does come with certain limitations. In order to fully understand the behaviour of a box type energy converter, a more realistic 3D model is essential. The study ignores turbulence, which might have some effect as well. The study also ignores mooring, which will play an essential role in motion control. Especially considering the shape and dimension of wave energy converters, mooring is essential to maintain their stability and perform a realistic study. Thus, addressing these limitations would be the principal focus in future studies.

Nevertheless, the study demonstrates that the open source CFD toolkit, OpenFOAM, is a promising tool for studying hydrodynamics of wave energy converters. Furthermore, the study also shows the capability of the linear analytical model in generating motion response results, confirming that the analytical model might be a very promising tool for initial design study. The study also demonstrates the potential of CFD modelling, to investigate the interaction between water waves and wave energy converters in a 3D wave flume.

Acknowledgements

This work was performed within the Project MIDWEST, Multi-fidelity Decision making tools for Wave Energy Systems, which is financed by the Portuguese Foundation for Science and Technology as part of the OCEANERA program. The second author has been contracted as a Researcher by the Portuguese Foundation for Science and Technology (Fundação para a Ciência e a Tecnologia), through Scientific Employment Stimulus, Individual support under the Contract No. CEE-CIND/04879/2017. The third author has been funded by the University of Lisbon and CENTEC with a PhD grant.

References

- Abul-Azm, A.G., Gesraha, M.R., 2000. Approximation to the hydrodynamics of floating pontoons under oblique waves. *Ocean. Eng.* 27, 365–384. [https://doi.org/10.1016/S0029-8018\(98\)00057-2](https://doi.org/10.1016/S0029-8018(98)00057-2).
- Abul-Azm, A.G., Williams, A.N., 1997. Oblique wave diffraction by segmented offshore breakwaters. *Ocean. Eng.* 24 (1), 63–82. [https://doi.org/10.1016/0029-8018\(95\)00065-8](https://doi.org/10.1016/0029-8018(95)00065-8).
- Antonini, A., Lamberti, A., Archetti, R., Miquel, A.M., 2016. Dynamic overset rans simulation of a wave-driven device for the oxygenation of deep layers. *Ocean. Eng.* 127, 335–348. <https://doi.org/10.1016/j.oceaneng.2016.10.016>.
- Antonini, A., Lamberti, A., Archetti, R., Miquel, A.M., 2016. CFD investigations of OXYFLUX device, an innovative wave pump technology for artificial downwelling of surface water. *Appl. Ocean Res.* 61, 16–31. <https://doi.org/10.1016/j.apor.2016.10.002>.
- Bhattacharjee, J., Guedes Soares, C., 2011. Oblique wave interaction with a floating structure near a wall with stepped bottom. *Ocean. Eng.* 38 (13), 1528–1544. <https://doi.org/10.1016/j.oceaneng.2011.07.011>.
- Bihs, H., Kamata, A., Lu, Z.J., Arntsen, I.A., 2017. Simulation of floating bodies using a combined immersed boundary with the level set method in REEF3D. In: Visonneau, M., Queutey, P., Le Touzé, D. (Eds.), VII Int'l Conf. On Computational Methods in Marine Eng. MARINE 2017.
- Black, J.L., Mei, C.C., Bray, M.C.G., 1971. Radiation and scattering of water waves by rigid bodies. *J. Fluid Mech.* 46, 151–164. <https://doi.org/10.1017/S0022112071000454>.
- Chen, L.F., Sun, L., Zang, J., Hillis, A., 2014. Numerical Simulation of Wave-Induced Roll of a 2-D Rectangular Barge Using OpenFOAM. 29th Int'l Workshop on Water Waves and Floating Bodies, Osaka, Japan.
- Connell, K.O., Cashman, A., 2015. Mathematical and CFD Analysis of Free Floating Heave-Only Body. 4th Int'l Con. on Renewable Energy Res. and Appl., Palermo, Italy <https://doi.org/10.1109/ICRERA.2015.7418456>.
- Drimer, N., Agnon, Y., Stiassnia, M., 1992. A simplified analytical model for a floating breakwater in water of finite depth. *Appl. Ocean Res.* 14 (1), 33–41. [https://doi.org/10.1016/0141-1187\(92\)90005-5](https://doi.org/10.1016/0141-1187(92)90005-5).
- Drobyshevski, Y., 2004. Hydrodynamic coefficients of a two-dimensional, truncated rectangular floating structure in shallow water. *Ocean. Eng.* 31, 305–341. <https://doi.org/10.1016/j.oceaneng.2003.07.004>.
- Devolder, B., Rauwoens, P., Troch, P., 2017. Numerical simulation of an array of heaving floating point absorber wave energy converters using OpenFOAM. In: Visonneau, M., Queutey, P., Le Touzé, D. (Eds.), VII Int'l Conf. On Computational Methods in Marine Eng. MARINE 2017.
- Gadelho, J.F.M., Mohapatra, S.C., Guedes Soares, C., 2017. CFD analysis of a fixed floating box-type structure under regular waves. In: Guedes Soares, C., Teixeira, A.P. (Eds.), Development in Maritime Transportation and Harvesting of Sea Resources. Taylor & Francis Group, London, pp. 513–520.
- Guo, Y., Mohapatra, S.C., Guedes Soares, C., 2018. Wave interaction with a rectangular long floating structure over flat bottom. In: Guedes Soares, C., Santos, T.A. (Eds.), Progress in Maritime Technology and Engineering, vol. 2018. Taylor & Francis Group, London, pp. 647–654.
- Holmes, S., Bhat, S., Beynet, P., Sablok, A., Prislun, I., 2001. Heave plate design with computational fluid dynamics. *J. Offshore Mech. Arct. Eng.* 123 (1), 22–28. <https://doi.org/10.1115/1.1337096>.
- Hsu, H.H., Wu, Y.C., 1997. The hydrodynamic coefficients for an oscillating rectangular structure on a free surface with side wall. *Ocean. Eng.* 24 (2), 177–199. [https://doi.org/10.1016/0029-8018\(96\)00009-1](https://doi.org/10.1016/0029-8018(96)00009-1).
- Huang, Z., He, F., Zhang, W., 2015. A floating box-type breakwater with slotted barriers. *J. Hydraul. Res.* 52 (5), 720–727. <https://doi.org/10.1080/00221686.2014.888690>.

- Islam, H., Mohapatra, S.C., Guedes Soares, C., 2018. Comparisons of CFD, experimental and analytical simulations of a heaving box-type floating structure. In: *Progress in Maritime Engineering and Technology* – Guedes Soares & Santos, pp. 633–639. <https://doi.org/10.1201/9780429505294-70>.
- ITTC – Recommended Procedures and Guidelines, 2008. Uncertainty analysis in CFD verification and validation methodology and procedures. Report ITTC 7.5-03-01-01.
- Jacobsen, N.G., Fuhrman, D.R., Fredsøe, J., 2012. A wave generation toolbox for the open-source CFD library: OpenFOAM. *Int. J. Numer. Methods Fluids* 70 (9), 1073–1088. <https://doi.org/10.1002/fld.2726>.
- Jasak, H., 2009. OpenFOAM: open source CFD in research and industry. *Int. J. Nav. Arch. Ocean. Eng.* 1 (2), 89–94. <https://doi.org/10.2478/IJNAOE-2013-0011>.
- Jaswar, K., Siow, C.L., Khairuddin, N.M., Abyn, H., Guedes Soares, C., 2015. Comparison of floating structures motion prediction between diffraction, diffraction-viscous and diffraction-Morison methods. In: Soares, Guedes, Santos (Eds.), *Maritime Technology and Engineering*. Taylor & Francis Group, London, pp. 1145–1152.
- Jung, J.H., Yoon, H.S., Chun, H.H., Lee, I., Park, H., 2013. Numerical simulation of wave interacting with a free rolling body. *Int. J. Nav. Arch. Ocean. Eng.* 5, 333–347. <https://doi.org/10.2478/IJNAOE-2013-0137>.
- Lee, J.F., 1995. On the heave radiation of the rectangular structure. *Ocean. Eng.* 22 (1), 19–34. [https://doi.org/10.1016/0029-8018\(93\)E0009-H](https://doi.org/10.1016/0029-8018(93)E0009-H).
- Lavrov, A., Guedes Soares, C., 2016. Modelling the heave oscillations of vertical cylinders with damping plates. *Int. J. Marit. Eng.* 158 (A3), 187–197. <https://doi.org/10.3940/rina.ijme.2016.a3.365>.
- Losada, I.J., Losada, M.A., Roldan, A.J., 1992. Propagation of oblique incident waves past rigid vertical thin barriers. *Appl. Ocean Res.* 14 (3), 191–199. [https://doi.org/10.1016/0141-1187\(92\)90014-B](https://doi.org/10.1016/0141-1187(92)90014-B).
- Mohapatra, S.C., Islam, H., Guedes Soares, C., 2019. Wave diffraction by a floating fixed truncated vertical cylinder based on Boussinesq equations. In: Guedes Soares, C. (Ed.), *Advances in Renewable Energies Offshore*. Taylor & Francis Group, London, pp. 281–289.
- Mohapatra, S.C., Guedes Soares, C., 2015. Wave forces on a floating structure over flat bottom based on Boussinesq formulation. In: Guedes Soares, C. (Ed.), *Renewable Energies Offshore*. Taylor & Francis Group, London, pp. 335–342.
- Ngina, P.M., Manyanga, D.O., Njenga, K.J., 2015. Wave exciting force on a floating rectangular barge due to surface waves. *Int. J. Sci. Eng. Res.* 6 (6), 1480–1485. ISSN 2229-5518.
- Nematbakhsh, A., Gao, Z., Moan, T., 2017. Benchmarking of a Computational Fluid Dynamics-based numerical wave tank for studying wave load effects on fixed and floating offshore structure. *J. Offshore Mech. Arct. Eng.* 139 (3), 1–11. <https://doi.org/10.1115/1.4035475>, 031301.
- Paci, A., Gaeta, M.G., Antonini, A., Archetti, R., 2016. 3D-numerical analysis of wave-floating structure interaction with OpenFOAM. In: *Proc. Int'l Offshore and Polar Eng. Conf.* 2016, pp. 1034–1039.
- Paci, A., Archetti, R., 2018. Application of a new OpenFOAM tool to design a pilot floating wind farm offshore mazara del vallo (Italy). In: *Proc. 28th Int'l Ocean and Polar Eng. Con. ISOPE 2018*, pp. 456–461.
- Philip, N.T., Nallayarasu, S., Bhattacharyya, S.K., 2013. Experimental investigation and CFD simulation of heave damping effects due to circular plates attached to spar hull. *Ships Offshore Struct.* 14 (4), 396–411. <https://doi.org/10.1080/17445302.2013.835146>.
- Rodriguez, M., Spinneken, J., Swan, C., 2016. Nonlinear loading of a two-dimensional heaving box. *J. Fluids Struct.* 60, 80–96. <https://doi.org/10.1016/j.jfluidstructs.2015.11.001>.
- Rodriguez, M., Spinneken, J., 2016. A laboratory study on the loading and motion of a heaving box. *J. Fluids Struct.* 64, 107–126. <https://doi.org/10.1016/j.jfluidstructs.2016.05.001>.
- Sannasiraj, S.A., Sundar, V., Sundaravadevelu, R., 1995. The hydrodynamic behavior of long floating structures in directional seas. *Appl. Ocean Res.* 17 (4), 233–243. [https://doi.org/10.1016/0141-1187\(95\)00011-9](https://doi.org/10.1016/0141-1187(95)00011-9).
- Williams, A.N., Lee, H.S., Huang, Z., 2000. Floating pontoon breakwater. *Ocean. Eng.* 27, 221–240. [https://doi.org/10.1016/S0029-8018\(98\)00056-0](https://doi.org/10.1016/S0029-8018(98)00056-0).
- Zheng, Y.H., Shen, Y.M., You, Y.G., Wu, B.J., Jie, D.S., 2006. Wave radiation by a floating rectangular structure in oblique seas. *Ocean. Eng.* 33, 59–81. <https://doi.org/10.1016/j.oceaneng.2005.04.005>.